Alloyed transition-metal dichalcogenides ($Mo_{1-x}W_xSe_2$) through a hydrothermal synthesis route: Probing layer-number-dependent band energies and band-gap bowing via scanning tunneling spectroscopy

Arpan Bera,[1,*] Biswajit Kundu,[1,*] Uttam Kumar Ghorai,[2] and Amlan J. Pal[1,3,†]

[1]*School of Physical Sciences, Indian Association for the Cultivation of Science, Kolkata 700032, India*

[2]*Department of Industrial & Applied Chemistry, Swami Vivekananda Research Center, Howrah, West Bengal 711202, India*

[3]*UGC-DAE Consortium for Scientific Research, University Campus, Khandwa Road, Indore 452001, India*

(Received 1 November 2022; accepted 9 January 2023; published 26 January 2023)

In this work, we form alloyed transition-metal dichalcogenides (TMDs), $Mo_{1-x}W_xSe_2$, through a hydrothermal synthesis procedure. Due to the identical effective ionic radius of the cations, the common-anionic alloys did not experience any lattice strain. A complete series of the common-anionic TMD alloys could thereby be synthesized; their nanosheets were formed by a liquid exfoliation method. The electronic properties of the alloyed nanosheets in their monolayer, bilayer, and trilayer forms were recorded separately through scanning tunneling spectroscopy (STS) in an extremely localized manner. From the STS studies, which have a correspondence to the density of states of the semiconductors, we have deliberated on their electronic properties and commented on the band edges of the nanosheets in the alloy series. The transport gap of the alloys in their monolayer, bilayer, and trilayer forms exhibited band-gap bowing, and also a layer-number-dependent bowing coefficient. That is, the bowing phenomenon interestingly occurred only in the few-layered TMD alloys and diminished to finally vanish in thicker nanosheets. The conduction band has been found to be responsible for such a nonlinear behavior of the transport gap; the results could be explained in terms of the molecular orbitals which form the band. The results have established a coherent description of the band-gap tuning in atomically thin 2D TMD alloys.

DOI: 10.1103/PhysRevMaterials.7.014005

I. INTRODUCTION

Transition-metal dichalcogenides (TMDs) have received a great deal of attention in a variety of applications due to their interesting light-matter interactions [1–4]. They possess a layered structure bound through a van der Waals (vdW) force between the layers and accordingly exhibit thickness-dependent physical phenomena. For example, their band gap changes from an indirect nature in multilayered nanosheets to a direct one in the monolayer limit [5,6]. The TMDs that are primarily studied have an MY_2 form where M represents a transition metal, such as Mo or W, and Y is a chalcogen amongst S, Se, and Te [7–9]. This has led to compounds like MoS_2, $MoSe_2$, and $MoTe_2$, and their tungsten counterparts for studies on their electronic properties and device characteristics thereof.

In recent years, alloyed TMDs have been studied in depth for such properties [1]. The identical symmetry of the crystal structure in different TMDs made it possible to form mixed-alloy systems with an adjustable band gap that is often phase-separation-free [10,11]. In the series of alloyed TMDs, $MoS_{2(1-x)}Se_{2x}$ was the first proposed material using density-functional theory (DFT) calculations; the mixed TMDs were referred to as 2D random alloys [12]. Soon, other alloys in the series, such as $MY_{2(1-x)}Y'_{2x}$ (M = Mo, W, and Y, $Y' = S$, Se, Te) were proposed and a phase diagram was drawn to show a bowing in the lattice constant due to a lattice mismatch between the anionic constituents (the effective ionic radii of S^{4-}, Se^{4-}, and Te^{4-} are 184, 198, and 221 pm, respectively); by employing the cluster expansion method and the special quasirandom structure approach, the alloys in their monolayer form were proposed to possess a continuously tunable direct band gap along with bowing in the band gap [13]. Monolayers of such materials were accordingly formed through a chemical vapor deposition (CVD) method and a superlinear composition-dependent photocurrent was observed in the devices based on the alloys [14].

Soon, alloying at the metal site was proposed [15,16]; $Mo_{1-x}W_xS_2$ single crystals were grown by the chemical vapor transport method. Although $Mo_{1-x}W_xS_2$ alloys possess a minimal lattice mismatch (effective ionic radii of Mo^{4+} and W^{4+} are 65 and 66 pm, respectively), their photoluminescence characteristics showed a band-gap engineering with tunable emission [15]. DFT studies in such materials inferred a band-gap bowing phenomenon in the monolayer of $Mo_{1-x}W_xS_2$ and attributed lowest unoccupied molecular orbital (LUMO) bowing to be the rationale of such a behavior [15]. Optical spectroscopy studies also yielded a bowing behavior in the optical band gap [17,18], although they probed the ensemble of the nanosheets on a larger area. Since the band gaps of the TMDs and alloyed TMDs vary with the layer number, optical spectroscopy would hence yield convoluted results clubbing the properties from different number of layers. Moreover, they will provide the optical band gap instead of the individual energies of the two band edges [17,18].

Electrical transport in a monolayer- and few-layered $Mo_{1-x}W_xS_2$ alloys was also investigated [19]. With

*These authors contributed equally to this work.

†sspajp@iacs.res.in

suppression of deep-level defects upon alloying [20], the $Mo_{1-x}W_xS(Se)_2$ alloys have possessed a minimal lattice mismatch and thereby an absence of lattice strain and spin-orbit engineering as well [21]. More recently, a few groups reported electronic properties of the alloyed TMDs on a localized scale through scanning tunneling spectroscopy (STS). STS studies of common-cationic alloys, $WS_{2(1-x)}Se_{2x}$ in their nanosheet forms, when grown through a physical vapor deposition (PVD) method, showed an inhomogeneous surface with respect to the WS_2 domain, WSe_2 domain, and defect-related areas [22]; such an inhomogeneity is expected due to a strain appearing due to a lattice mismatch between the constituents. In alloys of $Mo_xW_{1-x}S_2$ at the monolayer form, the binding energies exhibited a nonmonotonic behavior with the composition [23]. The $Mo_{1-x}W_xS(Se)_2$ alloys remained an ideal homogenous system for a range of optoelectronic applications since the constituents do not embed any lattice mismatch [24,25].

In the reports of $Mo_{1-x}W_xS_2$ and $Mo_{1-x}W_xS(Se)_2$ alloys [and $MY_{2(1-x)}Y'_{2x}$ as well], PVD, CVD, pulsed laser deposition, and molecular-beam epitaxy (MBE) methods were considered. In this context, a hydrothermal reaction, solvothermal treatment, and Schlenk line synthesis are among the most cost-effective and facile synthesis processes. We hence considered a hydrothermal synthesis procedure to form a complete series of common-anionic $Mo_{1-x}W_xSe_2$ alloys followed by liquid exfoliation to create nanosheets of the TMD alloys. Electronic properties of the series of TMDs, in their monolayer, bilayer, and trilayer forms, were probed separately in an extremely localized scale through STS to deliberate on their electronic properties. The STS studies have allowed us to comment on the band edges and a possible band-gap bowing of the nanoflakes as a function of their layer number. We have observed that the bowing effect is pronounced in the monolayered alloys and reduced with the growing number of layers. We accordingly have observed a layer-number-dependent band-gap bowing coefficient in the alloyed TMDs and thereby a complete description of band edges and band gap in the alloys.

II. MATERIALS AND METHODS

A. Materials

Selenium powder (99.99%), sodium tungstate dihydrate ($Na_2WO_4{\cdot}2H_2O$, $\geqslant$ 99.0%), sodium molybdate dihydrate ($Na_2MoO_4{\cdot}2H_2O$, $\geqslant$ 99.0%), and N-methyl-2-pyrrolidone (NMP, $\geqslant$ 99.0%) were purchased from Sigma-Aldrich Chemical Company. Sodium borohydride ($NaBH_4$, $\geqslant$ 95.0%) and N,N-dimethylformamide (DMF, $\geqslant$ 99.0%) were procured from Merck Life Science Private Limited. Cetyltrimethylammonium bromide (CTAB, > 98.0%) was bought from Tokyo Chemical Industry Co. Ltd. All of the compounds were stored in a nitrogen-filled glove box and used without additional purification.

B. Synthesis

The $Mo_{1-x}W_xSe_2$ powders were prepared by using a one-step hydrothermal process. As a selenium source, 0.4 g of selenium powder was dissolved in DMF along with 0.2 g of $NaBH_4$ and stirred for 2 h. Sodium molybdate dihydrate and sodium tungstate dihydrate in a measured ratio were dissolved in deionized water as the source of molybdenum and tungsten, respectively, and stirred for 2 h. CTAB was added to the thoroughly mixed solution and the stirring process was continued till the pH value exceeded 8.0. Thereafter, the mixed solution was placed in a Teflon-lined hydrothermal autoclave and kept at 220 °C for 48 h. The autoclave was then cooled to room temperature and the solution was filtered. A black precipitate could be collected and washed with deionized water and ethanol several times. The black powder was collected and dried in a 60 °C oven for 24 h. Finally, the samples were annealed in a nitrogen atmosphere at 400 °C for 3 h to improve their crystallinity. By varying the ratio between the molybdenum and tungsten sources, we have formed the $Mo_{1-x}W_xSe_2$ series with a targeted $x = 0.2$, 0.4, 0.6, and 0.8 apart from the end members, that is, $MoSe_2$ and WSe_2.

The alloyed TMDs and the end members were exfoliated in a 500-W probe sonicator operated at a frequency of 20 kHz; a cycle time of 11 s with a duty cycle of 73% was used to exfoliate the TMD powders, which were dispersed in 20 mL of NMP (2 mg/mL). For each composition, the sonication process was continued for 10 h; the temperature of the centrifuge tube used for the sonication was kept below 5 °C throughout the exfoliation process. The dispersion was then allowed to settle overnight. The top three-fourths of the supernatant were slowly decanted and then centrifuged at 2500 rpm for 15 min. Finally, the supernatant was collected for further investigation towards morphological and spectroscopic characterizations of the TMD nanoflakes.

C. Characterization

The exfoliated alloyed TMDs were characterized through usual routes. X-ray diffraction (XRD) patterns of $Mo_{1-x}W_xSe_2$ in their powder forms were recorded with a Rigaku SmartLab x-ray diffractometer equipped with a Cu Kα ($\lambda = 1.54$ Å) source. Their Raman spectra were recorded in a Horiba Jobin Yvon Raman triple-grating spectrometer system (model No. T64000); a diode-pumped solid-state laser provided 532.0 nm (power density of 0.5 mW μm^{-2}) as the excitation source. The size distribution and morphology of the nanosheets exfoliated from the bulk powder samples were studied using a JEOL transmission electron microscope (TEM) operated at 200 kV. For TEM imaging of the exfoliated nanosheets, a drop of their ultradilute dispersion was put on carbon-coated copper grids and dried in vacuum overnight. The nanosheets of the alloyed TMDs were also characterized using x-ray photoelectron spectroscopy (XPS) with Omicron XPS equipment (serial No. 0571).

Scanning tunneling spectroscopy of the alloyed TMDs in their nanosheet forms was recorded in ambient conditions using a scanning tunneling microscope (STM, Nanosurf easyscan 2). As the bottom electrode, a highly oriented pyrolytic graphite (HOPG) was used. A drop of the dispersion in NMP containing the nanosheets was cast on a freshly cleaved HOPG substrate; they were dried overnight in a nitrogen-filled glove box. The STM tips were formed through an oblique cut of a Pt/Ir (80:20) wire having a diameter of 0.25 mm. The tip was approached under a feedback loop to achieve a

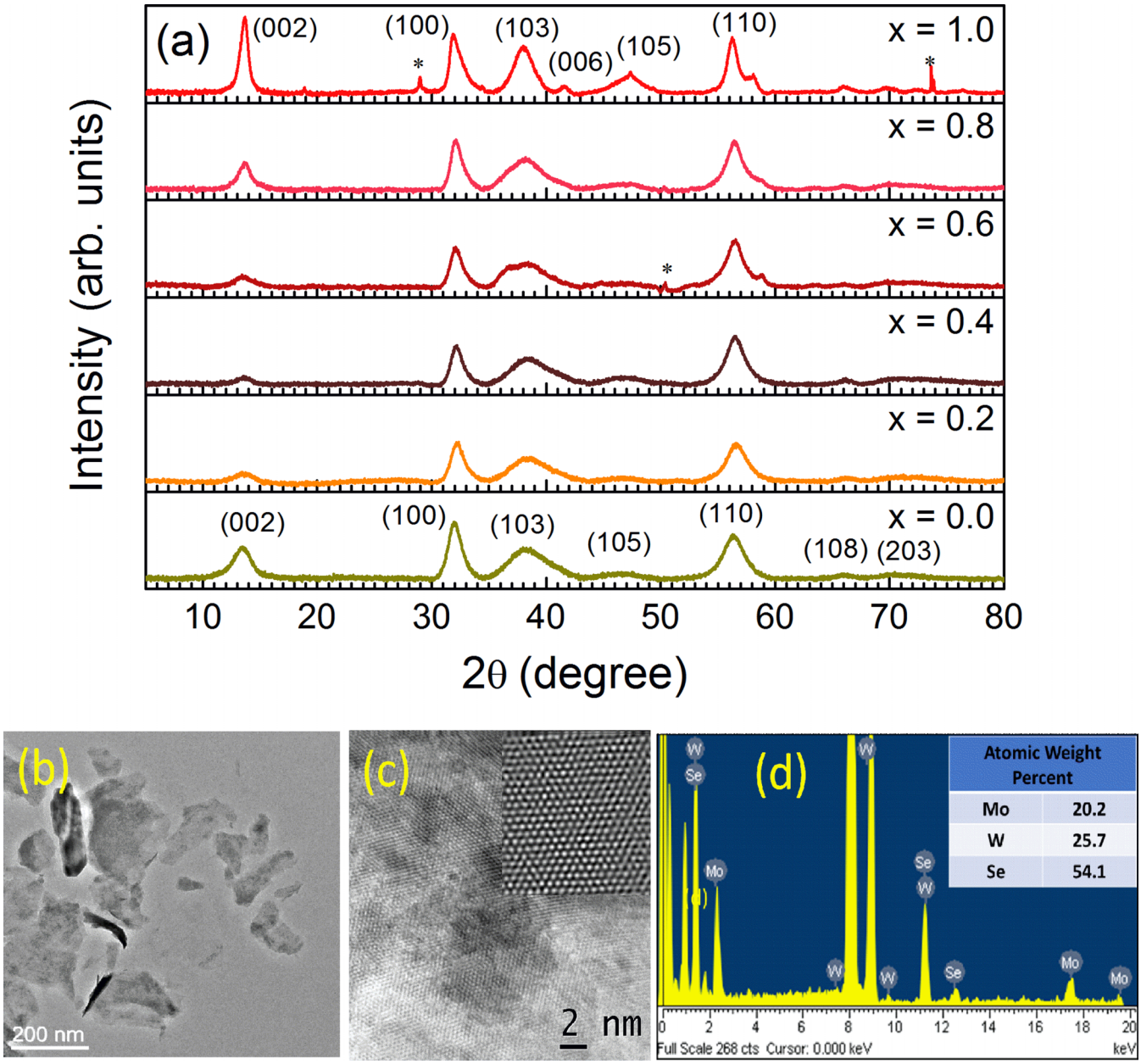

FIG. 1. (a) XRD patterns of $Mo_{1-x}W_xSe_2$ for different tungsten contents targeted during the synthesis process. (b) TEM image (with a targeted tungsten content, $x = 0.6$), and (c) (HR)-TEM image of the alloyed TMD. Inset of (c) shows the simulated atomic pattern by using GATAN software. (d) EDX spectrum of the $Mo_{1-x}W_xSe_2$ ($x = 0.6$) nanoflakes with the elements' atomic percentages.

set current of 0.5 nA at 1.5 V; the set point minimized the tip-induced band-bending effect which often perturbs the band edges. STM topographies were recorded at a constant current mode at the tip-approach condition. Tunneling current versus voltage characteristics (I–V) were recorded in the -2.0 V to $+2.0$ V region upon disabling the feedback loop. Differential tunnel conductance (dI/dV) spectra were derived from the I–V characteristics. Since monolayered, bilayered, trilayered, and multilayered sheets were formed during the exfoliation process, line profiles were drawn on each nanosheet prior to recording tunneling current versus voltage characteristics. With the thickness of a monolayer of $MoSe_2$ and WSe_2 being known, the line profiles provided the number of layers in a nanosheet before STS was derived on that particula sheet.

III. RESULTS AND DISCUSSION

Figure 1(a) shows the XRD patterns of $Mo_{1-x}W_xSe_2$ (targeted $x = 0.0, 0.2, 0.4, 0.6, 0.8$, and 1.0) powders. The alloyed TMDs, like the end members of the series, were crystalline and had returned significant patterns with clear peak positions. The crystalline phases of $MoSe_2$ and WSe_2 are consistent with earlier reports for the hexagonal phase of the TMDs [26,27]. Since they have mostly identical crystal structures and space groups, they have returned similar spectra. The alloys accordingly also yielded indistinguishable patterns implying the absence of other phases with the metals and the chalcogen. The full width at half maximum of the peaks also did not vary; the alloyed TMDs and the end members formed through the

hydrothermal process had hence similar crystallite sizes. The results hence imply the success of the hydrothermal synthesis process in forming the alloyed TMDs.

The microstructures and chemical markup of the exfoliated TMD nanosheets were investigated using TEM images. Figure 1(b) shows a typical TEM image of 2D $Mo_{1-x}W_xSe_2$ (with a targeted tungsten content, $x = 0.6$) nanosheets and the distribution of random-shaped flakes indicating that the liquid exfoliation process was successful in forming a large number of nanosheets. The images of other nanosheets have been placed in the left column of Fig. S1 in the Supplemental Material [28]. The image clearly demonstrates that the flakes were in the domain of ∼100 nm and less. Such smaller flakes were formed during the liquid exfoliation process due to a breakdown of intralayer covalent bonds in addition to the untying of the weak interlayer van der Waals force between the layers. When a nanosheet was probed for a high-resolution (HR)-TEM image [Fig. 1(c)], the crystalline character of the alloyed TMD could be seen in the form of distinctive lattice planes. The separation between arrays of atoms was 2.87 Å, which is consistent with the reported results [29].

To know the constituent components of the exfoliated TMD alloys, we recorded energy dispersive x-ray (EDX) spectroscopy. Figure 1(d) and the right column of Fig. S1 (Supplemental Material [28]) show EDX spectra and the atomic percentages of molybdenum, tungsten, and selenium in the exfoliated nanosheets. The achieved atomic percentages, which mostly matched the targeted percentage for all the alloys, have been tabulated in Table S1 in the Supplemental Material [28]. The achieved atomic percentages are being used for further deliberations. The distribution of the three elements for a particular alloy composition has been presented in Fig. S2 in the Supplemental Material [28]. The results provide compelling evidence towards the formation of alloys through the hydrothermal synthesis process.

The formation of $Mo_{1-x}W_xSe_2$ alloys was further confirmed by Raman spectroscopy. Figure 2(a) shows the Raman spectra for the $Mo_{1-x}W_xSe_2$ alloys with all compositions ($x = 0.0$ to 1.0 in steps of 0.2). While $MoSe_2$ returned its signature peak at 238.7 cm^{-1}, which represents the out-of-plane A_{1g} mode, WSe_2 exhibited the mode at 250.1 cm^{-1}. The results match the reports from the respective materials formed through other synthesis methods [30]. In fact, the frequencies could be fitted to a modified random-element-isodisplacement model and would yield composition-dependent force constants. In the Raman spectra of the alloys, the vibration of the A_{1g} mode could be seen to shift monotonically [Fig. 2(b)]. Appearance of a single peak in the alloys (rather than two peaks of the end members) and the peak shifting linearly with the alloy composition imply that $Mo_{1-x}W_xSe_2$ alloys indeed formed instead of a $MoSe_2$-WSe_2 two-phase system. Even when the tungsten content was as high as 0.39 or 0.56, the signature of $MoSe_2$ or WSe_2 did not appear in the Raman spectra. The spectra hence show the success of the alloyed-TMDs' formation through the hydrothermal synthesis route.

To deliberate if the valence states of the elements applicable in $MoSe_2$ and WSe_2 were retained in the alloys and the dichalcogenides were indeed formed, we present the XPS spectrum of a typical alloy, $Mo_{1-x}W_xSe_2$ with $x = 0.56$ (Fig. S3 in the Supplemental Material [28]). While a survey

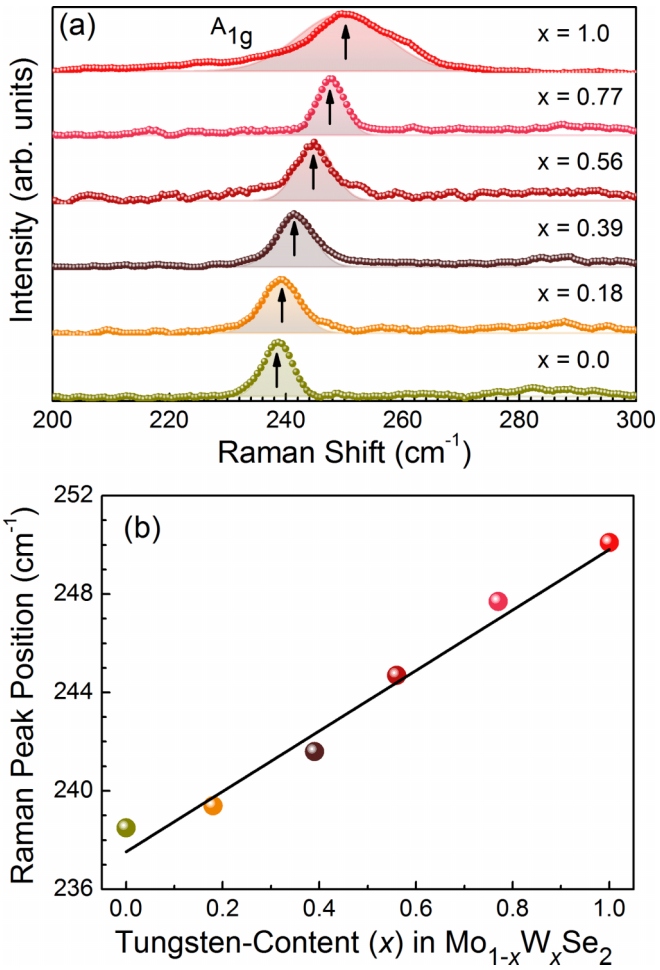

FIG. 2. (a) Raman spectra of $Mo_{1-x}W_xSe_2$ alloys with different tungsten contents. (b) Shift of the out-of-plane A_{1g} mode as a function of the tungsten content achieved in the alloys.

spectrum is shown in Fig. S3(a), high-resolution spectra in regions representing binding energies of molybdenum, tungsten, and selenium are shown in Figs. S3(b) through S3(d). The survey spectrum shows peaks representing binding energies of the three elements and also of the adventitious carbon. The high-resolution spectra yield (1) definite peaks of Mo(*IV*) $3d_{5/2}$ and $3d_{3/2}$ at 228.7 and 231.8 eV, respectively; (2) prominent peaks at 32.3, 34.4, and 37.9 eV representing W(*IV*) $4f_{7/2}$, $4f_{5/2}$, and $5p_{3/2}$, respectively; and (3) binding energies of Se $3d_{5/2}$ and $3d_{3/2}$, which are attributed to divalent selenium ions, at 54.3 and 55.1 eV, respectively. The XPS analysis thereby confirms the presence of molybdenum, tungsten, and selenium in the alloy; the analysis also infers that the valence state of binary TMDs was retained in the $Mo_{1-x}W_xSe_2$ alloy as well.

We then put the nanosheets of the alloyed TMDs in an STM to probe their density of states (DOS). We kept in mind that the exfoliation process resulted in nanosheets having different thicknesses: monolayers, bilayers, trilayers, and also higher number of layers. We also kept in mind that the electronic properties of the TMDs depend on the layer number in the nanoflakes [31,32]. In STM, since individual nanosheets are

probed in an extremely localized manner, we first determined their thickness. To do so, we recorded the STM topography of nanoflakes for each composition of the alloyed TMDs. We then drew line profiles on the STM topography of each nanoflake. The thickness of a nanosheet provided an estimate of the number of layers in the nanosheet. Expectedly, the thickness was found to be a multiple of the monolayer's thickness. Since the thickness of a monolayer of $MoSe_2$ or WSe_2 is known to be in the 0.6–0.7-nm range, we could thereby select a monolayer (or a bilayer or a trilayer) to probe their DOS. In Fig. 3(a), we present STM topographies of monolayers as evidenced from line profiles on the nanoflakes [Fig. 3(b)]. In the figures, we have clubbed images for all compositions, that is, $Mo_{1-x}W_xSe_2$ for all the achieved tungsten contents, and their line profiles. Atomic resolution images of the nanoflakes have also been added in the respective images. The images show that the material possessed the anticipated periodicity and structure. The line profiles on STM topographies allowed us to determine the thickness of a monolayer. In Fig. 3(c), we have plotted the thickness as a function of tungsten content in the alloy. The figure clearly shows that the thickness of the monolayer ranged between 0.67 and 0.73 nm. In the same manner, bilayered- and trilayered nanoflakes were selected to probe their DOS. STM topographies, high-resolution images, line profiles, and composition-dependent thickness of bilayers and trilayers are shown in Figs. S4 and S5 in the Supplemental Material [28], respectively. While the thickness of bilayered nanoflakes varied between 1.22 and 1.35 nm, the trilayers had a thickness ranging from 2.02 to 2.13 nm, as inferred from line profiles on STM topographies.

Upon identifying monolayered nanoflakes through the line profiles of STM topographies, we have recorded tunneling current versus voltage characteristics on those nanoflakes. Such characteristics enabled us to probe the electronic properties of each individual nanosheet. From the tunneling current spectroscopy, we have derived differential tunnel conductance (dI/dV) versus tip-voltage characteristics, which have a correspondence to the DOS of the semiconductors. As the bias was applied to the tip, the first peak in the positive voltage spectrum closest to 0 V (corresponding to Fermi energy, E_F) inferred the withdrawal of electrons from the semiconductor and thus its valence-band (VB) edge. Similarly, the first peak in the negative voltage closest to 0 V indicated electron injection to an available energy level of the material, that is, the conduction-band (CB) edge [33,34]. Each dI/dV spectrum thereby provided a set of CB- and VB edges with respect to the E_F. To compensate for the extremely localized mode of measurement, we recorded STS at many different points on each nanoflake. We hence could obtain a set of CB- and VB energies. We thereby drew a histogram of the two energies; the bin size of the histograms was set to the square root of the number of data points, as is customary in statistics. The peak energies in the histograms finally provided the band edges of the nanoflakes with respect to the E_F, and also the type of electronic conductivity of the nanosheets.

In Fig. 4(a), we have collated one typical dI/dV spectrum for each alloy composition. The histograms of band energies are shown in Fig. 4(b). With E_F being aligned to 0 V, the plots show an n-type nature of electronic conductivity in $MoSe_2$. The conductivity turned to a p type in WSe_2. Such inferences were drawn from a comparison between the separations of CB- and VB edges from E_F. From the histograms, we could also derive the transport gap of the alloyed TMDs. For the end members and the alloys, the transport gap was higher than the reported optical band gap [35,36] due to the involvement of a high exciton binding energy in the latter parameter. In Fig. 4(c), we have plotted the transport gap as a function of tungsten content in the alloys. The gap increased from 1.90 eV in $MoSe_2$ to 2.48 eV in WSe_2. The transport gap of the monolayer matched well with those of the $MoSe_2$ and WSe_2 nanosheets formed using the MBE method [37,38]. The values are much higher than that of possible air-induced adsorbates [39] on the nanoflakes, ruling out their effect in the measurements. The variation of the transport gap was quadratic in nature. The transport gap of an alloy was lower than that expected from a linear relationship. Such behavior is termed band-gap bowing and is seen as a deviation from Vegard's law, which states that the lattice parameter of a substitutional solid solution varies linearly between the lattice parameter values for the components. In the band gap of an alloy, a term is accordingly subtracted from the linear dependence as

$$E_g(x) = xE_g(1) + (1-x)E_g(0) - bx(1-x). \quad (1)$$

Here, the transport gap of an alloy $E_g(x)$ is related to the gap of the end members, $E_g(0)$ and $E_g(1)$ with "b" being the bowing coefficient.

Bowing in the band gap often arises due to lattice strain developed during the alloying process [13]. In the present system, the alloying process in forming $Mo_{1-x}W_xSe_2$ would not induce a lattice strain since the metals have nearly the same effective ionic radius (Mo^{4+}: 65 pm; W^{4+}: 66 pm). To deliberate on the rationale of the band-gap bowing in $Mo_{1-x}W_xSe_2$, we shall have to look at the orbitals responsible for forming the bands of the TMDs. The CB edge of the TMDs is usually formed with the d_z^2 orbitals of the cation (metal) and the p_x and p_y orbitals of the anion (chalcogen) atoms. The VB edge, on the other hand, is predominantly formed by the cation's d_{xy} and $d_{x^2-y^2}$ orbitals and the anion's p_x and p_y orbitals. Typically, the d_z^2 orbitals of the cation are the major contributor to the variation of the CB edge of the TMDs. The interaction between various cations is weak since the d_z^2 orbital spans along the out-of-plane-, that is, the z, direction. Due to lower energy of molybdenum's d_z^2 orbital than that of tungsten's, along with a limited intercation coupling, the CB edge of the alloys is localized to the molybdenum atoms even at very low molybdenum content [13,15]. As a result, even a small amount of molybdenum in the alloys causes the band gap of $Mo_{1-x}W_xSe_2$ to rapidly shift towards that of $MoSe_2$. Hence, the CB energy in the $Mo_{1-x}W_xSe_2$ alloy varies nonmonotonically and shifts quickly toward the CB edge of $MoSe_2$ [Fig. 4(d)]. Conversely, the d_{xy} and $d_{x^2-y^2}$ orbitals are strongly connected to each other since these states are extended in the x-y in-plane direction. Regardless of the constituents, such coupling delocalizes the wave function and causes the distribution of the VB edge to be nearly uniform over the cation content in the alloys. As a result, the VB energy tends to vary almost linearly with the tungsten composition [Fig. 4(d)]. Combining the nonlinear dependence of the

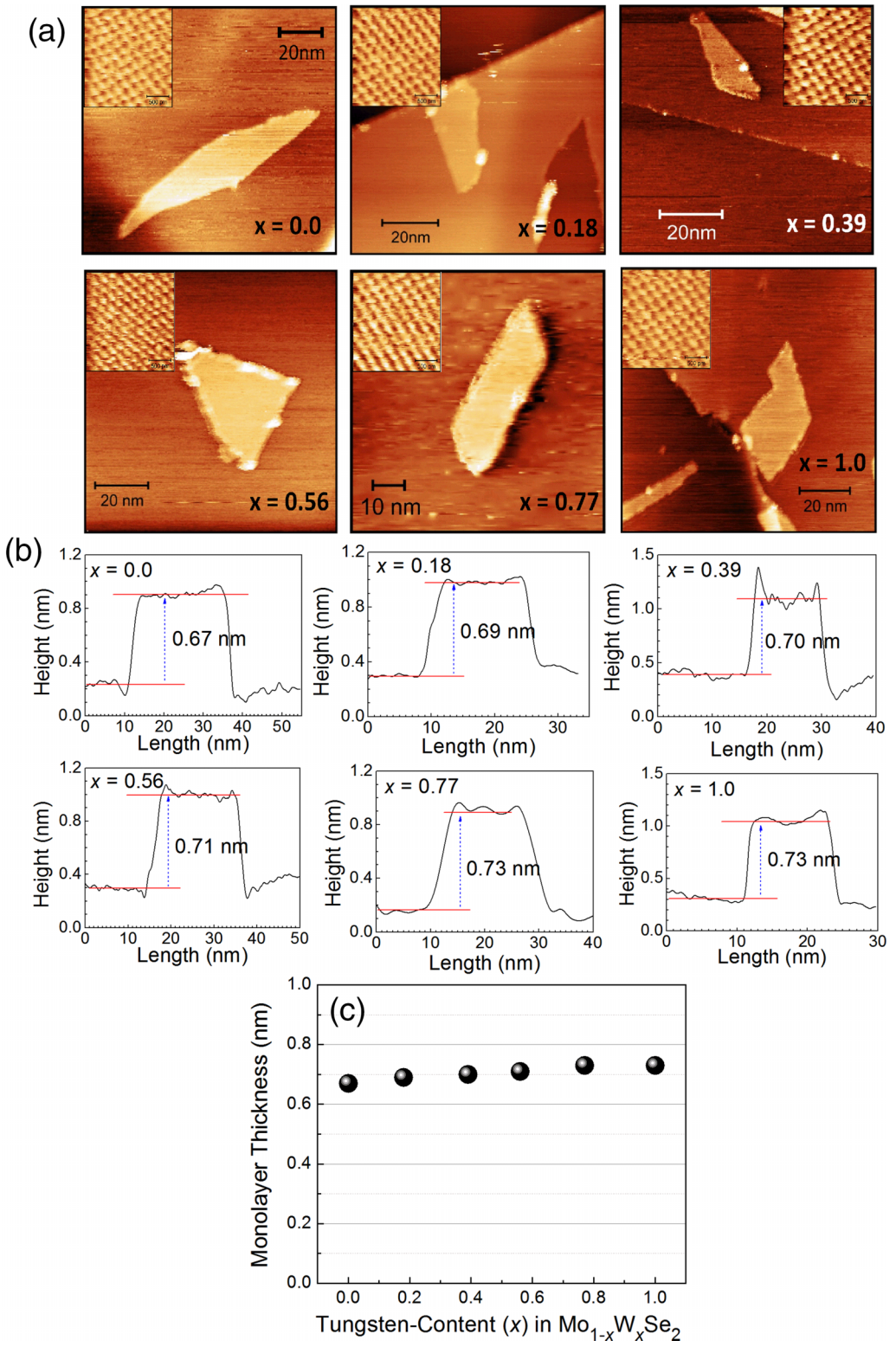

FIG. 3. (a) STM topographies of $Mo_{1-x}W_xSe_2$ nanoflakes in their monolayer form along with their atomic-resolution images. (b) Line profiles on the nanoflakes. The achieved tungsten content, *x,* has been quoted in the figures. (c) Thickness of a monolayer as a function of the achieved tungsten content.

CB edge and the linear behavior of the VB edge as a function of the tungsten content, the band gap of the $Mo_{1-x}W_xSe_2$ nanoflakes in their monolayer forms thereby displays a large band-gap bowing [Fig. 4(c)]. Within this context, our findings are quite intriguing since the $MoSe_2$ and WSe_2 are isostructural and the effective ionic radii of molybdenum and tungsten are nearly identical to cause any lattice strain in the alloys [40,41].

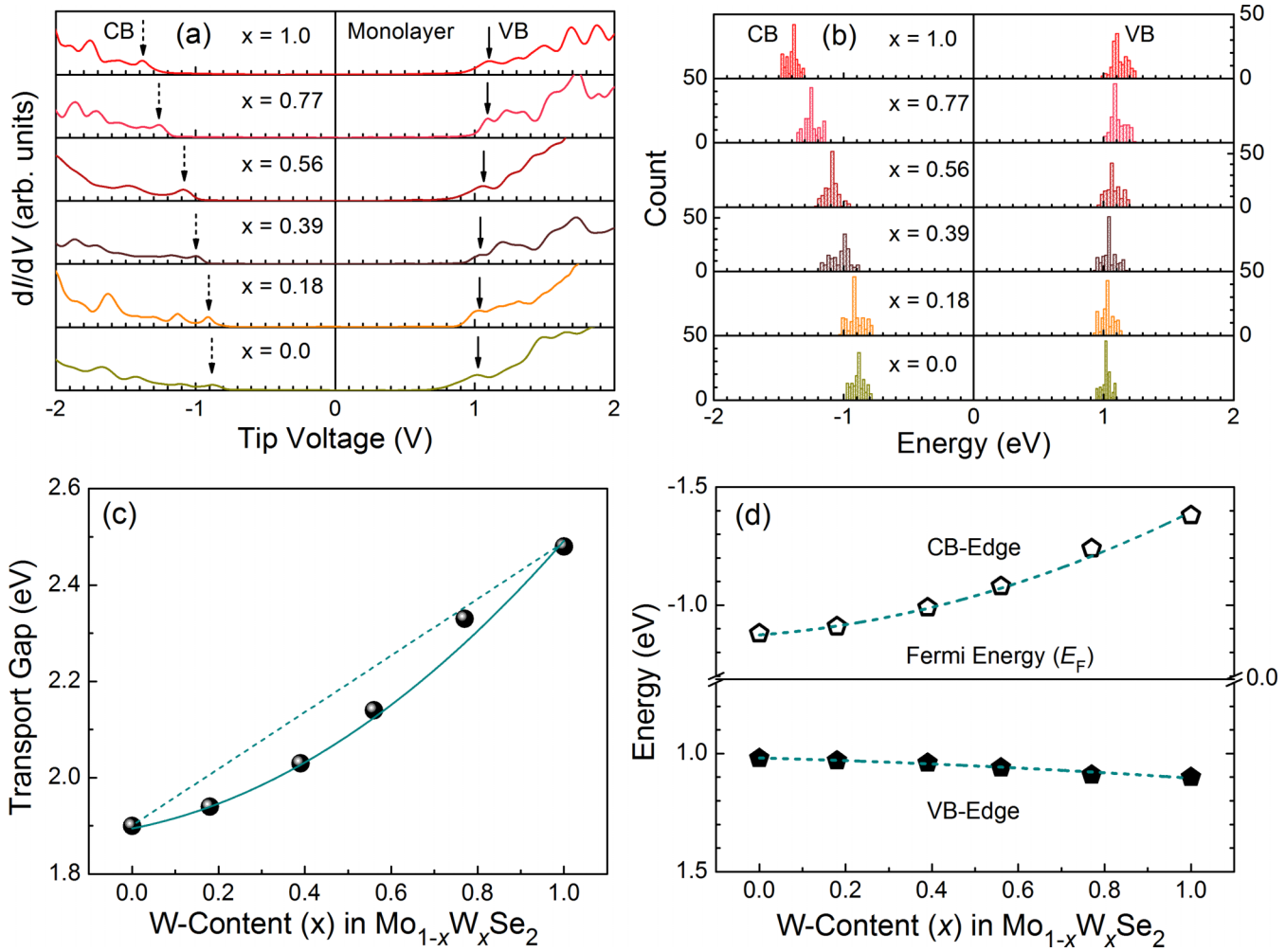

FIG. 4. (a) dI/dV vs tip voltage; (b) histogram of the CB and the VB energies with respect to Fermi energy (E_F) from STS studies of $Mo_{1-x}W_xSe_2$ monolayer nanosheets with varying tungsten content. (c) Variation of the transport gap with the achieved tungsten content in $Mo_{1-x}W_xSe_2$. The line represents a quadratic fit to the transport gap. (d) Composition dependence of CB and VB energies in the alloys with respect to the E_F.

Likewise, we have identified the bilayered and trilayered nanoflakes of the alloyed TMDs, separately. We have imaged STM topographies and identified the thickness of the nanoflakes from the line profiles. As stated, the thickness of bilayered nanoflakes varied from 1.22 to 1.35 nm; the trilayers had a thickness ranging from 2.02 to 2.13 nm, as inferred from line profiles on STM topographies. We then proceeded to measure the DOS of the semiconductors from tunneling current spectroscopy. In Figs. S6 and S7 in the Supplemental Material [28], we have provided one typical dI/dV spectrum for each alloy composition and the histograms of band energies for the bilayered and trilayered nanoflakes, respectively. The band edges were thereby derived from dI/dV spectroscopies and histograms of CB- and VB edges. In Fig. 5(a), we have presented the variation of the transport gap with the tungsten content in monolayered, bilayered, and trilayered $Mo_{1-x}W_xSe_2$ for comparison. The composition dependence of CB- and VB energies in the alloys with respect to the E_F is shown in Fig. 5(b). The figures show that the $MoSe_2$ nanoflakes retained their n-type nature in bilayered and trilayered nanoflakes as well; the WSe_2 nanoflakes similarly exhibited a p-type character. The transport gap in bilayered and trilayered alloys also yielded a band-gap bowing. The CB edge continued to contribute towards observing a band-gap bowing in the alloyed TMDs; the nonlinear dependence of the CB edge with the composition however weakened. The bowing parameter, b, accordingly decreased from 0.42 in monolayers to 0.04 in trilayers. It seems that the composition-dependent band gap turns to a linear relationship at thicker layers and in the bulk of the alloyed TMDs. A diminishing band-gap bowing in thicker nanoflakes may have arisen due to the involvement of d_z^2 orbitals of the cations (along the out-of-plane z direction) in determining the CB edge. In multilayered TMDs, the wave function delocalizes along the z direction and the variation of the CB edge hence turned linear with the tungsten composition. It may be recalled that the VB edge continued to vary linearly with the composition due to a delocalization of the wave function along the x-y plane. The transport gap of the alloys in their thicker nanoflakes hence tended to vary linearly with the composition.

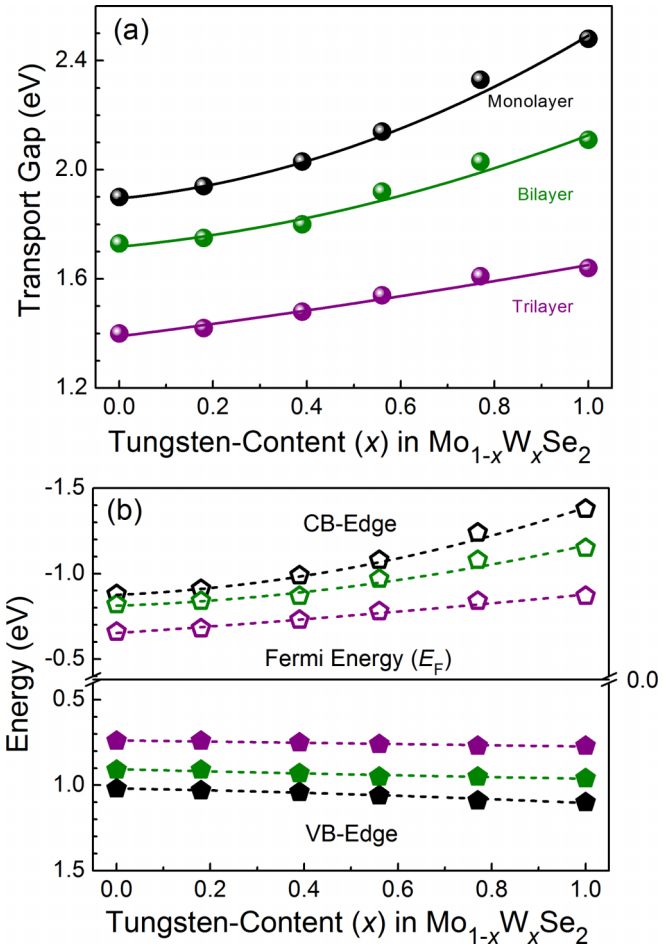

FIG. 5. (a) Variation of the transport gap with tungsten content in $Mo_{1-x}W_xSe_2$. Results from nanoflakes having monolayers, bilayers, and trilayers are being compared. The line represents a quadratic fit to each of the cases. (b) Composition dependence of CB- and VB energies in the alloys with respect to the E_F.

IV. CONCLUSION

In conclusion, we have successfully formed a series of $Mo_{1-x}W_xSe_2$ alloys through a hydrothermal synthesis route. The alloys were exfoliated to obtain nanoflakes which contained monolayers, bilayers, trilayers, and so forth. Through the localized nature of measurements in STS, we recorded the DOS of the nanoflakes in their monolayer, bilayer, and trilayer forms, separately. We accordingly derived CB- and VB edges of those nanoflakes and drew composition-dependent band edges and transport gaps of the alloyed TMDs. While $MoSe_2$ nanoflakes exhibited *n*-type conductivity, it changed to *p* type in the alloys and also in WSe_2 nanoflakes. In monolayered nanoflakes, the transport gap increased from 1.90 eV in $MoSe_2$ to 2.48 eV in WSe_2, nonlinearly. The transport gap exhibited a band-gap bowing as a deviation of Vegard's law. The bowing phenomenon interestingly occurred only in few-layered TMD alloys and diminished to finally vanish in thicker nanosheets. A complete band diagram in the common-anionic TMD alloys in their monolayer, bilayer, and trilayer forms has been drawn and the contribution of the two band edges in yielding the band-gap bowing has been derived. With the STS results showing that the VB in the alloys varied linearly with the composition, the bowing in the transport gap of such alloys has been explained in terms of the nonlinear dependence of the CB with the composition.

The data that support the findings in this paper are available from the corresponding author upon reasonable request.

ACKNOWLEDGMENTS

A.J.P. acknowledges JC Bose National Fellowship of SERB (Grant No. JBR/2021/000001) and the Asian Office of Aerospace Research and Development (AOARD) Grant No. FA2386-21-1-4031. A.B. acknowledges his INSPIRE Fellowship (Grant No. IF 190551) of DST.

The authors declare no competing financial interest.

[1] Q. H. Wang, K. Kalantar-Zadeh, A. Kis, J. N. Coleman, and M. S. Strano, Electronics and optoelectronics of two-dimensional transition metal dichalcogenides, Nat. Nanotechnol. **7**, 699 (2012).

[2] P. K. Sahoo, S. Memaran, F. A. Nugera, Y. Xin, T. D. Marquez, Z. G. Lu, W. K. Zheng, N. D. Zhigadlo, D. Smirnov, L. Balicas, and H. R. Gutierrez, Bilayer lateral heterostructures of transition-metal dichalcogenides and their optoelectronic response, ACS Nano **13**, 12372 (2019).

[3] Y. P. Liu, Y. J. Gao, S. Y. Zhang, J. He, J. Yu, and Z. W. Liu, Valleytronics in transition metal dichalcogenides materials, Nano Res. **12**, 2695 (2019).

[4] M. L. Tsai, S. H. Su, J. K. Chang, D. S. Tsai, C. H. Chen, C. I. Wu, L. J. Li, L. J. Chen, and J. H. He, Monolayer MoS_2 heterojunction solar cells, ACS Nano **8**, 8317 (2014).

[5] W. T. Zhang, X. D. Li, T. T. Jiang, J. L. Q. Song, Y. Lin, L. X. Zhu, and X. L. Xu, CVD synthesis of $Mo_{(1-x)}W_xS_2$ and $MoS_{2(1-x)}Se_{2x}$ alloy monolayers aimed at tuning the bandgap of molybdenum disulfide, Nanoscale **7**, 13554 (2015).

[6] A. Ciarrocchi, A. Avsar, D. Ovchinnikov, and A. Kis, Thickness-modulated metal-to-semiconductor transformation in a transition metal dichalcogenide, Nat. Commun. **9**, 919 (2018).

[7] Z. Y. Yin, H. Li, L. Jiang, Y. M. Shi, Y. H. Sun, G. Lu, Q. Zhang, X. D. Chen, and H. Zhang, Single-layer MoS_2 phototransistors, ACS Nano **6**, 74 (2012).

[8] H. L. Tang, M. H. Chiu, C. C. Tseng, S. H. Yang, K. J. Hou, S. Y. Wei, J. K. Huang, Y. F. Lin, C. H. Lien, and L. J. Li, Multilayer graphene-WSe_2 heterostructures for WSe_2 transistors, ACS Nano **11**, 12817 (2017).

[9] C. D. Ornelas, A. Bowman, T. S. Walmsley, T. J. Wang, K. Andrews, Z. X. Zhou, and Y. Q. Xu, Ultrafast photocurrent response and high detectivity in two-dimensional $MoSe_2$-based heterojunctions, ACS Appl. Mater. Interfaces **12**, 46476 (2020).

[10] Q. F. Gong, L. Cheng, C. H. Liu, M. Zhang, Q. L. Feng, H. L. Ye, M. Zeng, L. M. Xie, Z. Liu, and Y. G. Li, Ultrathin $MoS_{2(1-x)}Se_{2x}$ alloy nanoflakes for electrocatalytic hydrogen evolution reaction, ACS Catal. **5**, 2213 (2015).

[11] S. M. Oliver, R. Beams, S. Krylyuk, I. Kalish, A. K. Singh, A. Bruma, F. Tavazza, J. Joshi, I. R. Stone, S. J. Stranick, A. V. Davydov, and P. M. Vora, The structural phases and vibrational properties of $Mo_{1-x}W_xTe_2$ alloys, 2D Mater. **4**, 045008 (2017).

[12] H. P. Komsa and A. V. Krasheninnikov, Two-dimensional transition metal dichalcogenide alloys: Stability and electronic properties, J. Phys. Chem. Lett. **3**, 3652 (2012).

[13] J. Kang, S. Tongay, J. B. Li, and J. Q. Wu, Monolayer semiconducting transition metal dichalcogenide alloys: Stability and band bowing, J. Appl. Phys. **113**, 143703 (2013).

[14] V. Klee, E. Preciado, D. Barroso, A. E. Nguyen, C. Lee, K. J. Erickson, M. Triplett, B. Davis, I. H. Lu, S. Bobek, J. McKinley, J. P. Martinez, J. Mann, A. A. Talin, L. Bartels, and F. Leonard, Superlinear composition-dependent photocurrent in CVD-grown monolayer $MoS_{2(1-x)}Se_{2x}$ alloy devices, Nano Lett. **15**, 2612 (2015).

[15] Y. F. Chen, J. Y. Xi, D. O. Dumcenco, Z. Liu, K. Suenaga, D. Wang, Z. G. Shuai, Y. S. Huang, and L. M. Xie, Tunable band gap photoluminescence from atomically thin transition-metal dichalcogenide alloys, ACS Nano **7**, 4610 (2013).

[16] J. Y. Xi, T. Q. Zhao, D. Wang, and Z. G. Shuai, Tunable electronic properties of two-dimensional transition metal dichalcogenide alloys: A first-principles prediction, J. Phys. Chem. Lett. **5**, 285 (2014).

[17] Z. Wang, P. Liu, Y. Ito, S. Ning, Y. Tan, T. Fujita, A. Hirata, and M. Chen, Chemical vapor deposition of monolayer $Mo_{1-x}W_xS_2$ crystals with tunable band gaps, Sci. Rep. **6**, 21536 (2016).

[18] V. Murugan, K. Meganathan, N. B. Shinde, and S. K. Eswaran, Strain-mediated unusual bandgap bowing in continuous composition tuned monolayer $Mo_{1-x}W_xS_2$ ternary alloys, Appl. Phys. Lett. **118**, 013102 (2021).

[19] M. Zhang, J. X. Wu, Y. M. Zhu, D. O. Dumcenco, J. H. Hong, N. N. Mao, S. B. Deng, Y. F. Chen, Y. L. Yang, C. H. Jin, S. H. Chaki, Y. S. Huang, J. Zhang, and L. M. Xie, Two-dimensional molybdenum tungsten diselenide alloys: Photoluminescence, Raman scattering, and electrical transport, ACS Nano **8**, 7130 (2014).

[20] B. Huang, M. Yoon, B. G. Sumpter, S. H. Wei, and F. Liu, Alloy Engineering of Defect Properties in Semiconductors: Suppression of Deep Levels in Transition-Metal Dichalcogenides, Phys. Rev. Lett. **115**, 126806 (2015).

[21] G. Wang, C. Robert, A. Suslu, B. Chen, S. J. Yang, S. Alamdari, I. C. Gerber, T. Amand, X. Marie, S. Tongay, and B. Urbaszek, Spin-orbit engineering in transition metal dichalcogenide alloy monolayers, Nat. Commun. **6**, 10110 (2015).

[22] J. B. Peng, D. C. Yang, C. X. Ren, Y. Jiang, X. L. Zhu, F. L. Jing, H. L. Qiu, H. J. Liu, and Z. G. Hu, Electronic properties and carrier dynamics at the alloy interfaces of $WS_{2x}Se_{2-2x}$ spiral nanosheets, Adv. Mater. **34**, 2107738 (2022).

[23] A. F. Rigosi, H. M. Hill, K. T. Rim, G. W. Flynn, and T. F. Heinz, Electronic band gaps and exciton binding energies in monolayer $Mo_xW_{1-x}S_2$ transition metal dichalcogenide alloys probed by scanning tunneling and optical spectroscopy, Phys. Rev. B **94**, 075440 (2016).

[24] J. G. Song, G. H. Ryu, S. J. Lee, S. Sim, C. W. Lee, T. Choi, H. Jung, Y. Kim, Z. Lee, J. M. Myoung, C. Dussarrat, C. Lansalot-Matras, J. Park, H. Choi, and H. Kim, Controllable synthesis of molybdenum tungsten disulfide alloy for vertically composition-controlled multilayer, Nat. Commun. **6**, 7817 (2015).

[25] J. Park, M. S. Kim, B. Park, S. H. Oh, S. Roy, J. Kim, and W. Choi, Composition-tunable synthesis of large-scale $Mo_{1-x}W_xS_2$ alloys with enhanced photoluminescence, ACS Nano **12**, 6301 (2018).

[26] Y. Liu, M. Q. Zhu, and D. Chen, Sheet-like $MoSe_2$/C composites with enhanced Li-ion storage properties, J. Mater. Chem. A **3**, 11857 (2015).

[27] S. R. Kadam, A. N. Enyashin, L. Houben, R. Bar-Ziv, and M. Bar-Sadan, Ni-WSe_2 nanostructures as efficient catalysts for electrochemical hydrogen evolution reaction (HER) in acidic and alkaline media, J. Mater. Chem. A **8**, 1403 (2020).

[28] See Supplemental Material at http://link.aps.org/supplemental/10.1103/PhysRevMaterials.7.014005 for Table S1 and Figs. S1–S7 (TEM images, EDX spectra, and elemental mapping of $Mo_{1-x}W_xSe_2$ nanosheets at different tungsten contents, XPS spectra, STM topographies, differential conductance (dI/dV) spectra, and corresponding histograms of band positions in $Mo_{1-x}W_xSe_2$ nanosheets in their bilayer and trilayer forms).

[29] H. Bhunia and A. J. Pal, Band-edges and band-gap in few-layered transition metal dichalcogenides, J. Phys. D: Appl. Phys. **51**, 215102 (2018).

[30] P. Tonndorf, R. Schmidt, P. Bottger, X. Zhang, J. Borner, A. Liebig, M. Albrecht, C. Kloc, O. Gordan, D. R. T. Zahn, S. M. de Vasconcellos, and R. Bratschitsch, Photoluminescence emission and Raman response of monolayer MoS_2, $MoSe_2$, and WSe_2, Opt. Express **21**, 4908 (2013).

[31] J. Ji and J. H. Choi, Layer-number-dependent electronic and optoelectronic properties of 2D WSe_2-organic hybrid heterojunction, Adv. Mater. Interfaces **6**, 1900637 (2019).

[32] H. C. Kim, H. Kim, J. U. Lee, H. B. Lee, D. H. Choi, J. H. Lee, W. H. Lee, S. H. Jhang, B. H. Park, H. Cheong, S. W. Lee, and H. J. Chung, Engineering optical and electronic properties of WS_2 by varying the number of layers, ACS Nano **9**, 6854 (2015).

[33] O. Millo, D. Katz, Y. W. Cao, and U. Banin, Imaging and Spectroscopy of Artificial-Atom States in Core/Shell Nanocrystal Quantum Dots, Phys. Rev. Lett. **86**, 5751 (2001).

[34] D. Mocatta, G. Cohen, J. Schattner, O. Millo, E. Rabani, and U. Banin, Heavily doped semiconductor nanocrystal quantum dots, Science **332**, 77 (2011).

[35] A. Ramasubramaniam, Large excitonic effects in monolayers of molybdenum and tungsten dichalcogenides, Phys. Rev. B **86**, 115409 (2012).

[36] A. T. Hanbicki, M. Currie, G. Kioseoglou, A. L. Friedman, and B. T. Jonker, Measurement of high exciton binding energy in the monolayer transition-metal dichalcogenides WS_2 and WSe_2, Solid State Commun. **203**, 16 (2015).

[37] M. M. Ugeda, A. J. Bradley, S. F. Shi, F. H. da Jornada, Y. Zhang, D. Y. Qiu, W. Ruan, S. K. Mo, Z. Hussain, Z. X. Shen, F. Wang, S. G. Louie, and M. F. Crommie, Giant bandgap renormalization and excitonic effects in a monolayer transition metal dichalcogenide semiconductor, Nat. Mater. **13**, 1091 (2014).

[38] H. J. Liu, L. Jiao, L. Xie, F. Yang, J. L. Chen, W. K. Ho, C. L. Gao, J. F. Jia, X. D. Cui, and M. H. Xie, Molecular-beam epitaxy of monolayer and bilayer WSe_2: A scanning tunneling microscopy/spectroscopy study and deduction of exciton binding energy, 2D Mater. **2**, 034004 (2015).

[39] J. H. Park, S. Vishwanath, X. Liu, H. Zhou, S. M. Eichfeld, S. K. Fullerton-Shirey, J. A. Robinson, R. M. Feenstra, J. Furdyna, D. Jena, G H.. Xing, and A. C. Kummel, Scanning tunneling

microscopy and spectroscopy of air exposure effects on molecular beam epitaxy grown WSe_2 monolayers and bilayers, ACS Nano **10**, 4258 (2016).

[40] C. Ataca, H. Sahin, and S. Ciraci, Stable, single-layer MX_2 transition-metal oxides and dichalcogenides in a honeycomb-like structure, J. Phys. Chem. C **116**, 8983 (2012).

[41] J. Kang, S. Tongay, J. Zhou, J. B. Li, and J. Q. Wu, Band offsets and heterostructures of two-dimensional semiconductors, Appl. Phys. Lett. **102**, 012111 (2013).